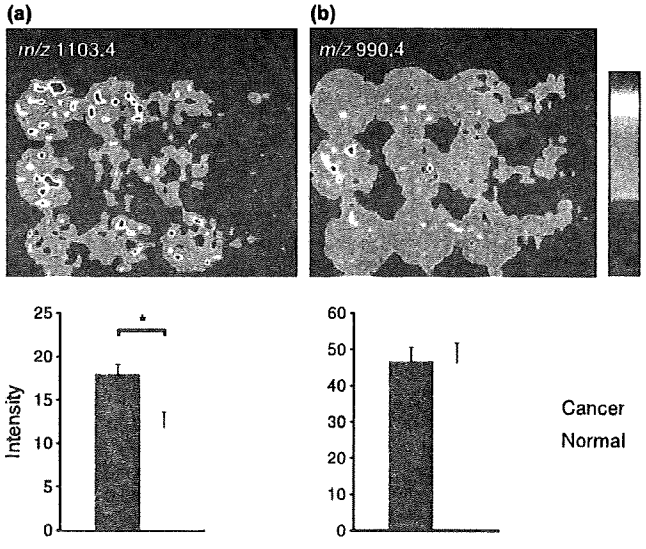

Fig. 4. Cancer-specific signal increase and even distribution of signals in imaging mass spectrometry (IMS) of digested formalin-fixed paraffin-embedded (FFPE) tissue microarrays (TMA). (a) Significantly strong peak intensity was detected at m/z 1103.4. (b) No significant difference was observed between cancer and normal tissues at an m/z of 990.4. Values are represented as mean ± SD (n = 3). $^*P < 0.05$.

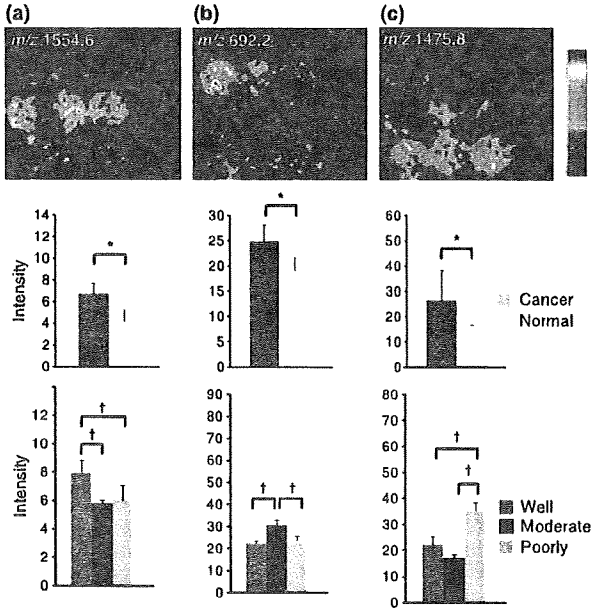

Fig. 5. Histological type-specific signal increase in imaging mass spectrometry (IMS) of digested formalin-fixed paraffin-embedded (FFPE) tissue microarrays (TMA). (a) Ion imaging revealed a peak with significantly strong signal intensity in well-differentiated adenocarcinoma at an m/z of 1554.6. (b) Ion imaging revealed a peak with significantly strong signal intensity in moderately differentiated adenocarcinoma at an m/z of 692.2. (c) Ion imaging revealed a peak with significantly strong signal intensity in poorly differentiated adenocarcinoma at m/z 1475.8. Values are represented as mean ± SD (n = 3). $^*P < 0.05$, $^\dagger P < 0.05$.

quantified the signal intensity using Scion image software. In agreement with our visual inspection, poorly differentiated carcinoma showed significantly higher value compared to well-

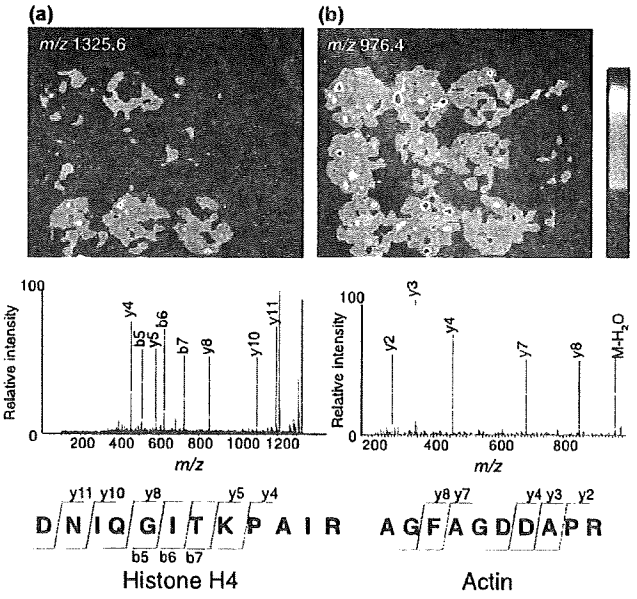

Fig. 6. MS/MS analysis of digested peptide and protein identification. (a) The biomolecule of an m/z 1325.6 was identified as histone H4. DNIQGITKPAIR: abbreviation of the amino-acid sequence aspartic acid–asparagine–isoleucine–glutamine–glycine–isoleucine–threonine–lysine–proline–alanine–isoleucine–arginine. y4, y5, y8, y10, y11 represent each fragment ion, which includes the C-terminal domain. b5, b6, b7 represent each fragment ion, which includes the N-terminal domain. (b) The biomolecule with an m/z 976.4 was identified as actin. AGFAGDDAPR: abbreviation for the amino-acid sequence alanine–glycine–phenylalanine–alanine–glycine–aspartic acid–aspartic acid–alanine–proline–arginine. y2, y3, y4, y7, y8 refer to each fragment ion, which includes the C-terminal domain.

differentiated or moderately differentiated carcinomas. There was no significant difference between well- and moderately differentiated carcinoma (Fig. 7c).

Discussion

In this report, we presented a simple and easy-to-use method for the detection and identification of cancer-specific proteins, i.e. strong candidates for biomarkers or drug targets, with high reliability in an experimental trial (Fig. 1). We succeeded in detecting cancer-specific signals with 75% (40 per 54) reliability in two independent experiments (Fig. 3, Fig. 4). Furthermore, we detected signals that were specific for each status of cancer differentiation (Fig. 5). Finally, we successfully identified one of the signals that was specifically increased in the poorly differentiated cancer tissue as histone H4 (Fig. 6).

We analyzed 12 different tissue samples within 1 h. The TMA-IMS technique has prominent advantages when compared to existing proteomic techniques. This technique enables the analysis of multiple proteins in multiple tissue samples in just one experiment. The existing proteomic techniques lack either multiprocessing property with respect to the analysis of samples or detection of proteins. Proteomic techniques employing 2D electrophoresis-MS or protein microarrays can analyze only single or double samples in one experiment; however, they can detect and identify multiple proteins in one experiment. In contrast, the limitation of TMA is that it enables that analysis of only one or two proteins in one experiment; however, it enables simultaneous analysis of multiple tissue samples. Thus, the TMA-IMS technique has two advantages compared to existing techniques. Moreover, the TMA-IMS technique does not require

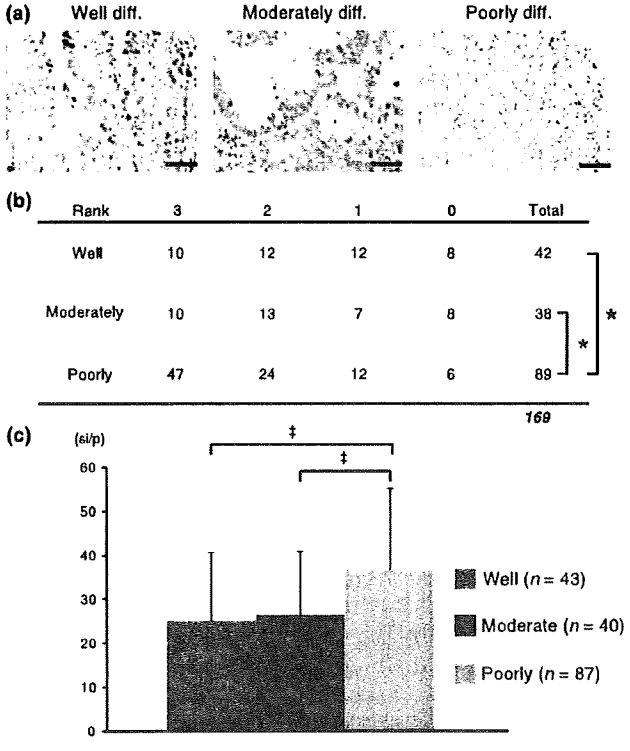

Fig. 7. Immunohistochemical (IHC) staining for histone H4. (a) Representative photomicrograph of IHC for histone H4 protein, ×400. Scale bar, 50 μm. (b) Evaluation of IHC according to four ranks (0, negative; 1, slightly positive; 2, positive; 3, strongly positive). The 169 gastric carcinomas comprised 42 well-differentiated carcinomas, 38 moderately differentiated carcinomas, 89 poorly differentiated carcinomas. *$P < 0.05$ by Steel–Dwass' test. (c) Quantitative analysis of IHC signal intensity. The 170 gastric carcinomas comprised 43 well-differentiated carcinomas, 40 moderately differentiated carcinomas, and 87 poorly differentiated carcinomas. Values are represented as mean ± SD. si/p, signal intensity per pixel. ‡$P < 0.01$.

the complicated sample-preparation steps which are required in 2-DE-MS-based proteomics.

The high-intensity signals detected from cancer tissues account for approximately two-thirds (54 of 72) of all signals detected. We failed to detect signals specific to normal tissues. This could be explained by the heterogeneity underlying normal tissues. The adjacent normal tissues consisted of varied types of tissues, such as mucosa, fatty tissue, and muscle. Acquired signal intensities in normal tissues were the average of whole spectrum derived from each of the tissues. Hence, tissue type-specific peaks were totally obscured, resulting in the failure to detect adjacent normal tissue-specific peaks.

We detected 17 histological type-specific peaks in two independent experiments. (Fig. 3) The reproducibility of signal detection from normal tissues was lower (4 per 17; 24%) than that of signal-detection from cancer tissues (75%). This could be explained by our experimental paradigm under which we performed two-step screening. The high severity of the first screening step excluded 9 of 13 peaks in either trial due to high variance among cancer tissues. In this technique, the two-step screening is essential as we cannot rule out the possibility of detecting false positive signals that are specific merely for certain patients. This problem could be addressed by spotting more samples under a variety of cancer tissue conditions in a TMA and performing multiple direct comparisons.

We identified from IMS screening histone H4 as a protein that is specifically increased in poorly differentiated adenocarcinoma (Fig. 6a). To validate the IMS result, we performed IHC for histone H4 protein using large amount of archival TMA specimens composed of various cellular density. In both visual inspection and quantitative analysis of IHC, histone H4 was strongly detected in poorly differentiated carcinoma (Fig. 7b,c). Similar strong detection of histone H4 in a cancer tissue has been reported by a recent study on a mouse model of brain tumor analyzed by IMS.[24] Dynamic chromatin remodeling such as DNA methylation, histone variants, covalent histone modifications, and ATP-dependent chromatin remodeling play important roles in carcinogenesis.[25,26] Indeed, poorly differentiated gastric adenocarcinoma is reported to lose Brm, a subunit of ATP-dependent chromatin-remodeling complex.[27] It can be assumed that these epigenetic changes lead to the chromatin-unfolding state and allow ready access to core histone protein. It might be also plausible that the higher cellular density of the poorly differentiated cancer tissues compared to other tissues explains the reason underlying the successful detection of a vast majority of histological type-specific signals from IMS. Conversely, signals specific to well- or moderately differentiated adenocarcinoma reflect the more-significant changes among the three histological types.

IMS technique was originally applied for the analysis of frozen tissue sections. FFPE samples are unsuitable for performing IMS due to the presence of cross-linkage between proteins and the inefficiency of enzyme digestion. Thus, few studies have reported the performance of IMS on FFPE samples.[28–30] Further, our study was hampered due to the disadvantage of FFPE. Due to the low S/N ratio, the identification of cancer- or histological type-specific proteins was rendered difficult.

TMA was originally used for IHC or *in situ* hybridization.[11,31] While this study was being conducted, another group reported the IMS of lung tumor biopsy in FFPE-TMA samples.[32] Thus, the FFPE-TMA-IMS has now emerged as the newest imaging technique. Other researchers have used this technique as an imaging tool to detect signals showing characteristic distribution in a particular tissue spot.[32] In contrast, we used the technique as a scanner for multiprocessing proteomics to readily detect cancer-specific signals. Two studies along these lines have reported highly different approaches. In this work, we loaded 12 tissue spots with 3-mm diameter in a TMA. Due to improvements in IMS resolution, the tissue spot size can now be reduced to submillimeter scales, enabling the loading of hundreds of tissue samples in one TMA. Thus, this technique can be applied for the analysis of a greater number of samples for high-throughput analysis of cancer characteristics.

Once a patient develops cancer, he or she should be subjected to medical treatments, including surgical operation and/or chemotherapy. To enable early detection of cancers, specific and sensitive biomarkers are desired. Using 2-DE based on MALDI mass spectrometry, potential proteins related to carcinogenesis have been discovered.[33,34] Further, in cases of far advanced or recurrent gastric carcinoma, chemotherapy prolongs the survival of the patient at a certain rate.[35] Proteomic analysis yielded an antidrug resistance agent,[36] while multidrug resistances were observed in certain cases. For retrospective evaluation and prospective searches of chemotherapy-related markers, high-throughput pathological evaluation methods are essential. IMS using TMA in FFPE, as we show here, will be one of the most promising gadgets in the surgical pathology laboratory.

In conclusion, we performed IMS of FFPE-TMA samples of gastric carcinoma, and successfully identified histone H4 as a signal specific to poorly differentiated cancer tissues. Moreover, the IMS-based finding was confirmed by IHC analyses of a large amount of TMAs. IMS of FFPE samples is a currently emerging

doi: 10.1111/j.1349-7006.2009.01384.x

technique and our experience represents an important step in the early phase of development. IMS of FFPE-TMA can offer fast and easy screening of cancer or tissue type-specific signals from a large amount of samples. The results of IMS-based screening can be readily verified by IHC analysis with other sets of FFPE-TMA samples. Combined with IHC confirmation, IMS of FFPE-TMA samples may be a further powerful tool in cancer proteomics.

Acknowledgments

This work was supported by a SENTAN step-up grant from JST to M.S. and by Grants-in-Aid from the Ministry of Health, Labour and Welfare for the Comprehensive 10-Year Strategy for Cancer Control (19-19) and the Third Term Comprehensive Control Research for Cancer; the Japan Society for the Promotion of Science for Scientific Research (no. 19790286), and the Smoking Research Foundation.

References

1 DeRisi J, Penland L, Brown PO *et al.* Use of a cDNA microarray to analyse gene expression patterns in human cancer. *Nat Genet* 1996 Dec; **14** (4): 457–60.
2 Ramsay G. DNA chips: state-of-the art. *Nat Biotechnol* 1998 Jan; **16** (1): 40–4.
3 Zhao X, Li C, Paez JG *et al.* An integrated view of copy number and allelic alterations in the cancer genome using single nucleotide polymorphism arrays. *Cancer Res* 2004 May 1; **64** (9): 3060–71.
4 Engle LJ, Simpson CL, Landers JE. Using high-throughput SNP technologies to study cancer. *Oncogene* 2006 Mar 13; **25** (11): 1594–601.
5 McLendon R, Friedman A, Bigner D *et al.* Comprehensive genomic characterization defines human glioblastoma genes and core pathways. *Nature* 2008 Oct 23; **455** (7216): 1061–8.
6 Ley TJ, Mardis ER, Ding L *et al.* DNA sequencing of a cytogenetically normal acute myeloid leukaemia genome. *Nature* 2008 Nov 6; **456** (7218): 66–72.
7 Hood L, Heath JR, Phelps ME, Lin B. Systems biology and new technologies enable predictive and preventative medicine. *Science* 2004 Oct 22; **306** (5696): 640–3.
8 Aebersold R, Mann M. Mass spectrometry-based proteomics. *Nature* 2003 Mar 13; **422** (6928): 198–207.
9 Diamandis EP. Mass spectrometry as a diagnostic and a cancer biomarker discovery tool: opportunities and potential limitations. *Mol Cell Proteomics* 2004 Apr; **3** (4): 367–78.
10 Sreekumar A, Nyati MK, Varambally S *et al.* Profiling of cancer cells using protein microarrays: discovery of novel radiation-regulated proteins. *Cancer Res* 2001 Oct 15; **61** (20): 7585–93.
11 Kononen J, Bubendorf L, Kallioniemi A *et al.* Tissue microarrays for high-throughput molecular profiling of tumor specimens. *Nat Med* 1998 Jul; **4** (7): 844–7.
12 Stoeckli M, Chaurand P, Hallahan DE, Caprioli RM. Imaging mass spectrometry: a new technology for the analysis of protein expression in mammalian tissues. *Nat Med* 2001 Apr; **7** (4): 493–6.
13 Shimma S, Sugiura Y, Hayasaka T, Zaima N, Matsumoto M, Setou M. Mass imaging and identification of biomolecules with MALDI-QIT-TOF-based system. *Anal Chem* 2008 Feb 1; **80** (3): 878–85.
14 Shimma S, Furuta M, Ichimura K, Yoshida Y, Setou M. Direct MS/MS analysis in mammalian tissue sections using MALDI-QIT-TOFMS and chemical inkjet technology. *Surf Interface Anal* 2006; **38** (2): 1712–14.
15 Groseclose MR, Andersson M, Hardesty WM, Caprioli RM. Identification of proteins directly from tissue: *in situ* tryptic digestions coupled with imaging mass spectrometry. *J Mass Spectrom* 2007 Feb; **42** (2): 254–62.
16 Crew KD, Neugut AI. Epidemiology of gastric cancer. *World J Gastroenterol* 2006 Jan 21; **12** (3): 354–62.
17 Japanese Gastric Cancer A. Japanese classification of gastric carcinoma – 2nd English edn. *Gastric Cancer* 1998 Dec; **1** (1): 10–24.
18 Schwartz SA, Reyzer ML, Caprioli RM. Direct tissue analysis using matrix-assisted laser desorption/ionization mass spectrometry: practical aspects of sample preparation. *J Mass Spectrom* 2003 Jul; **38** (7): 699–708.
19 Espada A, Rivera-Sagredo A. Ammonium hydrogencarbonate, an excellent buffer for the analysis of basic drugs by liquid chromatography-mass spectrometry at high pH. *J Chromatogr A* 2003 Feb 14; **987** (1–2): 211–20.
20 Wong JW, Cagney G, Cartwright HM. SpecAlign – processing and alignment of mass spectra datasets. *Bioinformatics* 2005 May 1; **21** (9): 2088–90.
21 Whistler T, Rollin D, Vernon SD. A method for improving SELDI-TOF mass spectrometry data quality. *Proteome Sci* 2007; **5**: 14.
22 Yanaga Y, Awai K, Nakaura T *et al.* Optimal contrast dose for depiction of hypervascular hepatocellular carcinoma at dynamic CT using 64-MDCT. *AJR Am J Roentgenol* 2008 Apr; **190** (4): 1003–9.
23 Lemaire R, Desmons A, Tabet JC, Day R, Salzet M, Fournier I. Direct analysis and MALDI imaging of formalin-fixed, paraffin-embedded tissue sections. *J Proteome Res* 2007 Apr; **6** (4): 1295–305.
24 Seeley EH, Caprioli RM. Molecular imaging of proteins in tissues by mass spectrometry. *Proc Natl Acad Sci USA* 2008 Nov 25; **105** (47): 18126–31.
25 Wang GG, Allis CD, Chi P. Chromatin remodeling and cancer, part I: covalent histone modifications. *Trends Mol Med* 2007 Sep; **13** (9): 363–72.
26 Wang GG, Allis CD, Chi P. Chromatin remodeling and cancer, part II: ATP-dependent chromatin remodeling. *Trends Mol Med* 2007 Sep; **13** (9): 373–80.
27 Yamamichi N, Inada K, Ichinose M *et al.* Frequent loss of Brm expression in gastric cancer correlates with histologic features and differentiation state. *Cancer Res* 2007 Nov 15; **67** (22): 10727–35.
28 Aoki Y, Toyama A, Shimada T *et al.* A novel method for analyzing formalin-fixed paraffin embedded (FFPE) tissue sections by mass spectrometry imaging. *Proc Jpn Acad Ser B* 2007; **83** (2): 205–14.
29 Stauber J, Lemaire R, Franck J *et al.* MALDI imaging of formalin-fixed paraffin-embedded tissues: application to model animals of Parkinson disease for biomarker hunting. *J Proteome Res* 2008 Mar; **7** (3): 969–78.
30 Ronci M, Bonanno E, Colantoni A *et al.* Protein unlocking procedures of formalin-fixed paraffin-embedded tissues: application to MALDI-TOF imaging MS investigations. *Proteomics* 2008 Sep; **8** (18): 3702–14.
31 Sugimura H. Detection of chromosome changes in pathology archives: an application of microwave-assisted fluorescence *in situ* hybridization to human carcinogenesis studies. *Carcinogenesis* 2008 Apr; **29** (4): 681–7.
32 Groseclose MR, Massion PP, Chaurand P, Caprioli RM. High-throughput proteomic analysis of formalin-fixed paraffin-embedded tissue microarrays using MALDI imaging mass spectrometry. *Proteomics* 2008 Sep; **8** (18): 3715–24.
33 Yoshihara T, Kadota Y, Yoshimura Y *et al.* Proteomic alteration in gastic adenocarcinomas from Japanese patients. *Mol Cancer* 2006; **5**: 75.
34 Cheng Y, Zhang J, Li Y, Wang Y, Gong J Proteome analysis of human gastric cardia adenocarcinoma by laser capture microdissection. *BMC Cancer* 2007; **7**: 191.
35 Ohtsu A. Chemotherapy for metastatic gastric cancer: past, present, and future. *J Gastroenterol* 2008; **43** (4): 256–64.
36 Wang X, Lu Y, Yang J *et al.* Identification of triosephosphate isomerase as an anti-drug resistance agent in human gastric cancer cells using functional proteomic analysis. *J Cancer Res Clin Oncol* 2008 Sep; **134** (9): 995–1003.

Supporting Information

Additional Supporting Information may be found in the online version of this article:

Fig. S1. The array images obtained with imaging mass spectrometry (IMS) are shown. There are 18 evenly distributed images and 37 cancer specific ones, two well-differentiated adenocarcinoma-specific images, one well- and moderately differentiated adenocarcinoma-specific image, two moderately differentiated adenocarcinoma-specific images, four moderately and poorly differentiated adenocarcinoma-specific images, and eight poorly differentiated adenocarcinoma-specific images. Values are represented as mean ± SD ($n = 3$). *$P < 0.05$. †$P < 0.05$.

Please note: Wiley-Blackwell are not responsible for the content or functionality of any supporting materials supplied by the authors. Any queries (other than missing material) should be directed to the corresponding author for the article.

Biosensors and Bioelectronics 25 (2009) 22–27

Contents lists available at ScienceDirect

Biosensors and Bioelectronics

journal homepage: www.elsevier.com/locate/bios

Development of a method to evaluate caspase-3 activity in a single cell using a nanoneedle and a fluorescent probe

Takanori Kihara[a,b], Chikashi Nakamura[c,d,*], Miho Suzuki[e], Sung-Woong Han[c], Kyoko Fukazawa[f], Kazuhiko Ishihara[a,b,f], Jun Miyake[a,b,c,d]

[a] The Center for NanoBio Integration, The University of Tokyo, 7-3-1, Hongo, Bunkyo-ku, Tokyo 113-8656, Japan
[b] Department of Bioengineering, School of Engineering, The University of Tokyo, 7-3-1, Hongo, Bunkyo-ku, Tokyo 113-8656, Japan
[c] Research Institute of Cell Engineering, National Institute of Advanced Industrial Science and Technology, Central 4, 1-1-1 Higashi, Tsukuba, Ibaraki 305-8562, Japan
[d] Department of Biotechnology and Life Science, Tokyo University of Agriculture and Technology, 2-24-16, Naka-cho, Koganei, Tokyo 184-8588, Japan
[e] Department of Functional Materials Science, Faculty of Engineering, Saitama Univeristy, 255 Shimo-okubo, Saitama, Saitama, 338-8570, Japan
[f] Department of Materials Engineering, School of Engineering, The University of Tokyo, 7-3-1, Hongo, Bunkyo-ku, Tokyo 113-8656, Japan

ARTICLE INFO

Article history:
Received 25 March 2009
Received in revised form 22 May 2009
Accepted 28 May 2009
Available online 6 June 2009

Keywords:
Nanoneedle
AFM
Single cell
FRET
Caspase-3 activity
MOMENT

ABSTRACT

A method to detect an enzymatic reaction in a single living cell using an atomic force microscope equipped with an ultra-thin needle (a nanoneedle) and a fluorescent probe molecule was developed. The nanoneedle enables the low-invasive delivery of molecules attached onto its surface directly into a single cell. We hypothesized that an enzymatic reaction in a cell could be profiled by monitoring a probe immobilized on a nanoneedle introduced into the cell. In this study, a new probe substrate (NHGcas546) for caspase-3 activity based on fluorescent resonance energy transfer (FRET) was constructed and fixed on a nanoneedle. The NHGcas546-modified nanoneedle was inserted into apoptotic cells, in which caspase-3 is activated after apoptosis induction, and a change in the emission spectrum of the immobilized probe could be observed on the surface of the nanoneedle. Thus, we have developed a successful practical method for detecting a biological phenomenon in a single cell. We call the method MOlecular MEter with Nanoneedle Technology (MOMENT).

1. Introduction

The direct manipulation and delivery of molecules into a single living cell would provide a novel technology that could be useful in biology, biotechnology, and medicine (Lamontagne et al., 2008; Voldman, 2006). There are two main applications of such molecular manipulation techniques: One is to regulate cell states (e.g., cell differentiation, cell reprogramming), and the other is to reveal the state or the type of a cell; the latter can be currently accomplished by investigating the operation of biological activities by analysing gene expression levels in the cell. For the advancement of these applications, molecular handling techniques with more spatial and temporal precision are required.

We have developed a novel molecular handling technique for a single cell using the atomic force microscope (AFM), which accurately measures the displacement and force exerted on a cantilever, and an ultra-thin needle (nanoneedle) to penetrate the cell membrane with minimal cell damage. Penetration with nanoneedles smaller than 400 nm in diameter does not cause lethal damage to the plasma membrane; because of their low invasiveness, the needles can be maintained inside the cell for more than 1 h for analysis (Han et al., 2005). Insertion of a nanoneedle through the plasma membrane can be monitored by determining the force exerted on the nanoneedle (Obataya et al., 2005c). This procedure allows us to deliver molecules that are attached onto the nanoneedle surface into the cell (Han et al., 2005; Obataya et al., 2005a).

Many kinds of fluorescent probes have been used to detect enzymatic activity (Miyawaki, 2003; Tsien, 2005). The sensing mechanism of such probes is usually based on fluorescent resonance energy transfer (FRET) between green fluorescent protein (GFP) and its colour variants for applications in the fields of cell biology, molecular biology, and developmental biology (Miyawaki, 2003; Pollok and Heim, 1999). In many cases, this system requires a construct such that an enzyme sensitive sequence is placed between two fluorescent proteins. Recently, a FRET-based system using an engineered GFP with a chemical FRET partner was reported. This chimeric FRET-based system aims to place the chemical fluorophore considerably close to and suitably oriented to GFP for efficient FRET using a site-directed mutagenesis approach (Suzuki et al., 2003, 2004).

* Corresponding author at: Research Institute of Cell Engineering, National Institute of Advanced Industrial Science and Technology, Central 4, 1-1-1 Higashi, Tsukuba, Ibaraki 305-8562, Japan. Tel.: +81 29 861 2445; fax: +81 29 861 3049.
E-mail address: chikashi-nakamura@aist.go.jp (C. Nakamura).

0956-5663/$ – see front matter © 2009 Elsevier B.V. All rights reserved.
doi:10.1016/j.bios.2009.05.036

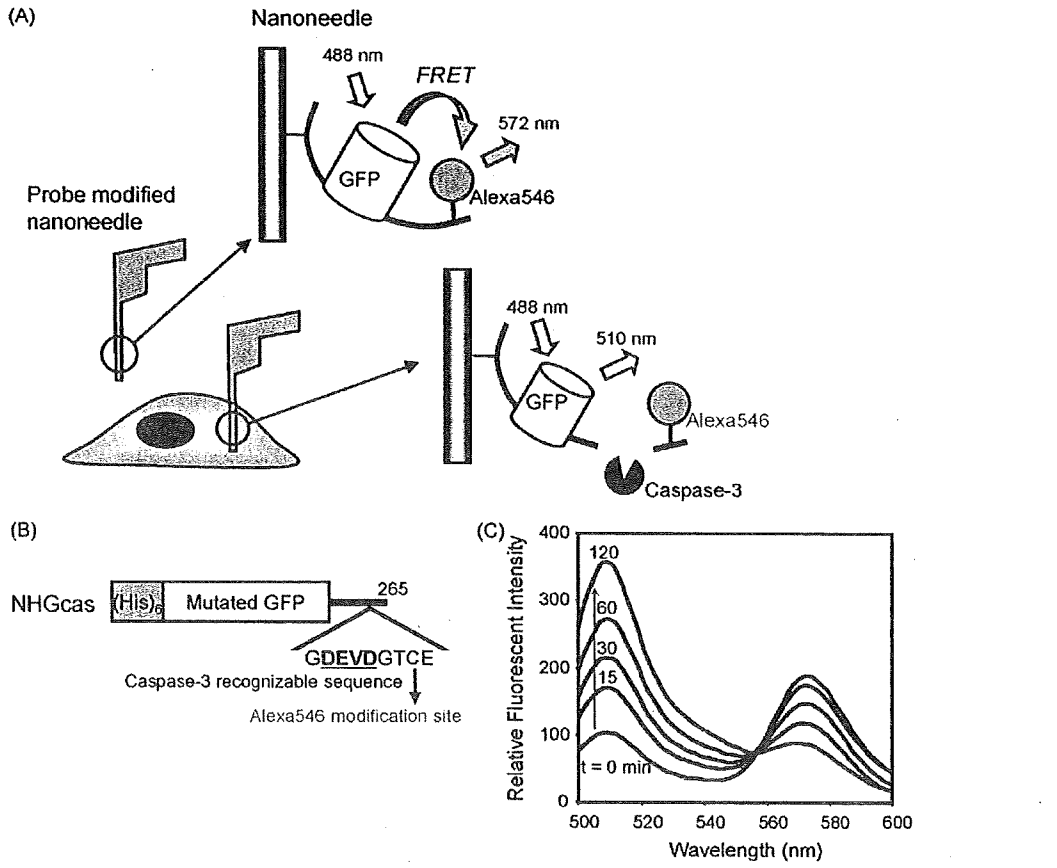

Fig. 1. Structure of the NHGcas546 probe. (A) Schematic diagram of the new biosensor for intracellular enzyme assay. A nanoneedle carrying immobilized probe molecules is inserted into a cell and the probe on the nanoneedle reacts with the enzyme inside the cell. The immobilized NHGcas546 probe emits at 572 nm upon excitation at 488 nm; after digestion with caspase-3 in an apoptotic cell, the immobilized NHGcas546 emits at 510 nm. (B) Primary structure of NHGcas. NHGcas was constructed using mutated GFP, a caspase-3 recognizable sequence (DEVD), and a Cys modified with Alexa Fluor 546. NHGcas has a $(His)_6$ tag at its N-terminus. (C) Emission spectra of NHGcas546 during digestion with recombinant caspase-3. NHGcas546 was incubated with caspase-3 for 120 min in solution. Excitation was at 488 nm. The fluorescence emission spectrum of the probe changed in caspase-3 solution and the intramolecular FRET signal was abolished in a time-dependent manner.

For the procedure, these fluorescent probes need to be expressed or introduced into the cells after fabrication by chemical or physiological methods. However, those introduction strategies have some restrictions on applicable cell types and growth conditions, and suffer from reduced viability after invasive damage. It is often difficult to employ these techniques in primary cultured cells or normal human cells. We have developed a molecular manipulation technique for a single cell that might have the potential to deliver many types of molecule into various cell types, including normal human cells, without invasive damage (Han et al., 2008). To combine this technique with the use of fluorescent chimeric probes, it is necessary to adapt the probes to function on the surface of the nanoneedle inside the cell. This combination scheme is based on the concept of a biosensor for real-time monitoring of biological phenomena in a single living cell (Fig. 1A).

In this study, a FRET-based probe (NHGcas546) functioning on a nanoneedle surface was developed to quantify the activity of caspase-3, a key enzyme of apoptosis. NHGcas546 consists of an engineered GFP with an N-terminal $(His)_6$ tag, a sequence (Asp-Glu-Val-Asp) recognizable by caspase-3 (Thornberry et al., 1997), and a cysteine for site-directed modification with an Alexa Fluor 546 dye at its C-terminus (Fig. 1B). The NHGcas546 was attached to the surface of the silicon cantilever by chelate bonding of the $(His)_6$ tag. This probe on an AFM cantilever was demonstrated to change its FRET signal as a result of cleavage by recombinant caspase-3. The NHGcas546 immobilized on a nanoneedle was then inserted into a single apoptotic cell assumed to express caspase-3 and a change in the emission spectrum was observed. Thus, the development of a new device like a micro-biosensor to investigate enzymatic activity in a single cell has been accomplished. We named the new method MOlecular MEter with Nanoneedle Technology (MOMENT). MOMENT allows the measurement of the activity of a desired molecule in a cell at that moment.

2. Materials and methods

2.1. Materials

AFM silicon cantilevers (CONT and ATEC-CONT) were purchased from Nanosensors (Neuchatel, Switzerland). The BCA protein assay kit and Halt EDTA-free protease inhibitor cocktail were purchased from Pierce Biotechnology (Rockford, IL). 2-Methacryloyloxyethyl phosphorylcholine (MPC) and *p*-nitrophenyloxycarbonyl poly(ethylene glycol) methacrylate (MEONP) were synthesized using previously reported methods (Ishihara et al., 1991; Konno et al., 2004). 3-Methacryloxypropyl triethoxysilane (MTES) was purchased from Shin-Etsu Chemical Co. Ltd. (Tokyo, Japan). Alexa Fluor 546 C5 maleimide was purchased from Invitrogen (Carlsbad, CA). TALON Metal Affinity Resin and *Escherichia coli* BL21(DE3)pLysS were purchased from Takara Bio Inc. (Shiga, Japan). NAP-10 desalting columns were purchased from GE Healthcare Life Sciences (Buckinghamshire, England).

Active human caspase-3 was purchased from Medical & Biological Laboratories Co. Ltd. (Nagoya, Japan). AB-NTA was purchased from Dojindo laboratories (Kumamoto, Japan). Other reagents were purchased from Wako Pure Chemical Industries Ltd. (Osaka, Japan) or Sigma–Aldrich (St. Louis, MO).

2.2. Plasmid construction

The protein part of the probe, called NHGcas, was derived from the GFP variant UV5casS02tag (Suzuki et al., 2005). The construction detail is described in Supplementary methods. The resulting construct was named pNHGcas.

2.3. Purification of NHGcas

E. coli BL21(DE3)pLysS was transformed with pNHGcas. LB medium supplemented with 34 μg/mL chloramphenicol, 100 μg/mL ampicillin, and 0.5-mM IPTG was inoculated with transformed *E. coli* in the growth phase and cultured at 26 °C for 3 h. The cells were harvested by centrifugation at 8000 × *g* for 15 min and resuspended in PBS. The cell suspension was suspended and vortexed with lysis buffer: PBS containing 10% glycerol, 0.5% Triton-X-100, and an EDTA-free protease inhibitor cocktail. The resulting lysate was sonicated and centrifuged at 8000 × g for 15 min. The supernatant was applied to a TALON Metal Affinity resin column. After serial washing with lysis buffer and modified lysis buffer supplemented with 2-mM imidazole, the NHGcas bound to the resin through its $(His)_6$ tag was eluted with lysis buffer containing 100-mM imidazole. The eluted protein was desalted on a NAP-10 gel permeation column. The desalted NHGcas was collected to determine its concentration with the BCA kit. Purified and quantified NHGcas was analyzed by 10% SDS-PAGE. The schematic structure of NHGcas is shown in Fig. 1B.

2.4. Preparation of the caspase-3 activity sensor probe

The caspase-3 sensor probe, NHGcas546, was prepared from NHGcas by chemical modification with Alexa Fluor 546. An aliquot of purified NHGcas dissolved in PBS containing 10% glycerol, 0.5% Triton-X-100, and 1-mM DTT was kept at room temperature for 15 min; thereafter, the remaining DTT was removed using a NAP-10 gel permeation column equilibrated with PBS. An aliquot of eluate was immediately mixed with 10 equivalent amounts of Alexa Fluor 546 C5 maleimide solution and incubated at 37 °C for 3 h. Excess fluorescent dye was removed by dialysis against PBS. The concentration of prepared NHGcas546 was determined using the BCA kit.

2.5. Preparation of nanoneedle

The nanoneedle was prepared by focused ion beam (SMI3050, SII Nanotechnology Co. Ltd., Chiba, Japan) etching as described previously (Obataya et al., 2005b). The pyramidal silicon AFM tip (ATEC-CONT, spring constant is about 0.2 N/m) was fabricated to a needle shape of approximately 400 nm in diameter and 10 μm in length with a flat-ended cylindrical edge.

2.6. Detection of caspase-3 activity in a single apoptotic cell

HeLa cells were maintained in DMEM containing 10% FBS, and antibiotics (100 units/mL penicillin G, 100 μg/mL streptomycin sulphate). Apoptosis was induced with 10 μg/mL cycloheximide and 100 ng/mL TNF-α. We performed Annexin V assays to confirm the induction of apoptosis (data not shown). Apoptotic HeLa cells were manipulated using a combination of confocal laser scanning microscopy (CLSM) (IX81/FV1000, Olympus, Tokyo, Japan) and AFM (Nanowizard I, JPK Instruments AG, Berlin, Germany). The NHGcas546 immobilized nanoneedle was inserted into an apoptotic cell aimed toward the centre of the cell by manual operation. The nanoneedle was maintained inside the cell for 60 min and then retracted. The fluorescence of NHGcas546 on the nanoneedle was examined by CLSM before and after the nanoneedle insertion. The images obtained were analyzed using ImageJ software (National Institutes of Health, Bethesda, MD, USA). The Young's modulus of the cell was calculated in accordance with the Hertz model (Obataya et al., 2005c). The force–distance curve (z-scan speed of 6 μm/s) at the region of indentation was fitted to the Hertz model. The following equation is used in the Hertz model of indentation for cylindrical material:

$$F = \frac{2aE}{(1-\nu^2)}I,$$

where F = force, I = depth of indentation, a = radius of nanoneedle, ν = Poisson's ratio (0.5), and E = Young's modulus.

All other methods used in this work are described in Supplementary methods.

3. Results and discussion

3.1. Design of a FRET-based probe for measuring caspase-3 activity on a silicon surface

A highly sensitive fluorescent probe that can function on a nanoneedle should be a powerful tool for *in situ* characterization of enzymatic activity in a single living cell. Since the nanoneedle was prepared from a single silicon AFM cantilever, the fluorescent probe should have a solid surface binding site and an enzyme-sensitive site. Thus, a new FRET-based probe composed of fluorescent protein and dye to measure caspase-3 activity was devised in this study (Fig. 1A).

This probe was attached to the nanoneedle via the N-terminus of the protein part to detect the activity of caspase-3 as a change in the emission spectrum of the probe; the protease sensitive site was located at the C-terminus of the protein part (Fig. 1B). We used GFP as the protein part and Alexa Fluor 546 as the fluorescent dye, as shown in Fig. 1B. This probe contained the DEVD sequence between GFP and Alexa Fluor 546, which is mainly cleaved by caspase-3 (Thornberry et al., 1997).

Fig. 1C shows the changes in emission profile of NHGcas546 digested with caspase-3 in solution. The emission around 510 nm from GFP clearly increased and the emission around 570 nm from Alexa Fluor 546 simultaneously decreased in a time-dependent manner (Fig. 1C). This suggests that NHGcas546 was cleaved by caspase-3 to abolish intramolecular FRET. The ratio of the fluorescence intensities at 572 and 510 nm was 1.83 at 0 min and 0.247 after 120 min after caspase-3 action. This gave a 7.4-fold alteration of the ratio by caspase-3 digestion. The alteration of the corresponding ratio on UV5casS22tag modified with Alexa Fluor 532 was 6.4 (Suzuki et al., 2005). Alexa Fluor 532 can be weakly excited at 488 nm, producing an unfavourable background for this analysis, but Alexa Fluor 546 is scarcely excited at this wavelength. Thus, NHGcas546 is a very effective probe of caspase-3 activity for further study.

3.2. Modification of a silicon surface with NHGcas546

Many points must be considered when building a probe on a nanoneedle surface to function in the interior of a cell. One consideration is the activity of the molecular probe on the nanoneedle surface for effectively sensing enzymatic activity. Another consideration is nonspecific adsorption onto the nanoneedle surface that would be an obstacle to molecular sensing. To overcome these

issues, a MPC polymer was used to modify the silicon surface (Kihara et al., 2007). The surface of MPC polymers has abundant free water molecules (Ishihara et al., 1998; Kitano et al., 2003). Thus, proteins are exposed to circumstances similar to a solution, meaning that their conformation does not change on the MPC polymer surface. Moreover, the surface of the MPC polymer has low protein adsorption. MPC is often used as a surface-modification polymer for various materials that come in contact with tissue or blood (Goda et al., 2006; Moro et al., 2004). For this study, because silicon surface bonding groups and active ester groups for immobilizing biomolecules were required in the polymer chain, MPC, MTES, and MEONP were copolymerized (Supplementary Fig. 1). MTES is a monomer for silane coupling and MEONP is a monomer with a reactive ester group (Konno et al., 2004).

First, the silicon AFM cantilever was modified with the MPC polymer by silane coupling. Thereafter, the *p*-nitrophenyl ester group was reacted with the amino group of AB-NTA to produce NTA groups on the surface. NTA is one of the most useful matrices for immobilized metal-affinity chromatography. A Ni^{2+} was chelated to the NTA group. The Ni^{2+}-NTA group can tightly bind a $(His)_6$ tagged protein. NHGcas546 was then supposed to attach to the Ni^{2+}-NTA group on the silicon AFM cantilever.

The silicon cantilever modified with NHGcas was observed by CLSM, and successful binding of the protein was confirmed (Supplementary Fig. 2). The amount of attached NHGcas was about 3×10^4 molecules/μm^2, or approximately 3 per 10-nm square. The diameter of the GFP barrel structure is about 24 Å (Ormo et al., 1996; Yang et al., 1996). Thus, it is estimated there could be approximately 20 closely packed molecules in each 10-nm square; the occupied fraction of NHGcas was about 15%. The surface area of the nanoneedle was 13 μm^2 at 400 nm diameter. Hence, about 4×10^5 molecules of NHGcas546 could be on the surface of the nanoneedle.

3.3. Cleavage of NHGcas546 with caspase-3 on the silicon surface

To evaluate the performance of the attached NHGcas546 probe on the silicon surface, the NHGcas546-modified silicon cantilever was treated with recombinant caspase-3 and was then observed by CLSM (LSM510-META) at 488 nm laser excitation and 511–599 nm emission.

The emission spectrum of NHGcas546 on the cantilever surface showed two distinct peaks: one from fluorescent protein and one from Alexa Fluor dye (Fig. 2a). The NHGcas546 on the surface of the cantilever clearly showed an intramolecular FRET spectrum pattern. When the probe was incubated with buffer alone, the emission spectrum of the NHGcas546 probe did not demonstrate significant change. However, the intensity of the fluorescence gradually decreased by sequential observation every 5 min (Fig. 2a). This suggests that the structure of NHGcas546 might be maintained on the MPC polymer-modified solid surface but its fluorescence would be bleached by continuous excitation.

Upon treatment with 1 unit of caspase-3 at room temperature, the emission of the NHGcas546 on the silicon surface clearly decreased around 570 nm (Fig. 2b). This indicated that the NHGcas546 was digested by caspase-3, thereby cancelling the intramolecular FRET signal.

Fig. 2c shows the time-dependent changes in the ratio of emission intensities of Alexa Fluor 546 (577–599 nm)/fluorescent protein (513–534 nm) on the silicon cantilever. The emission ratio was normalized by defining the baseline ratio at 0 min of caspase-3 treatment. The rate constant of 1 unit caspase-3 action on the NHGcas546 attached to the silicon cantilever was 5.4×10^{-4}/s. The ratio of the fluorescence intensity of Alexa Fluor 546/fluorescent protein after treatment with caspase-3 was 0.59. This gave a 1.7-fold alteration of the ratio by caspase-3 digestion.

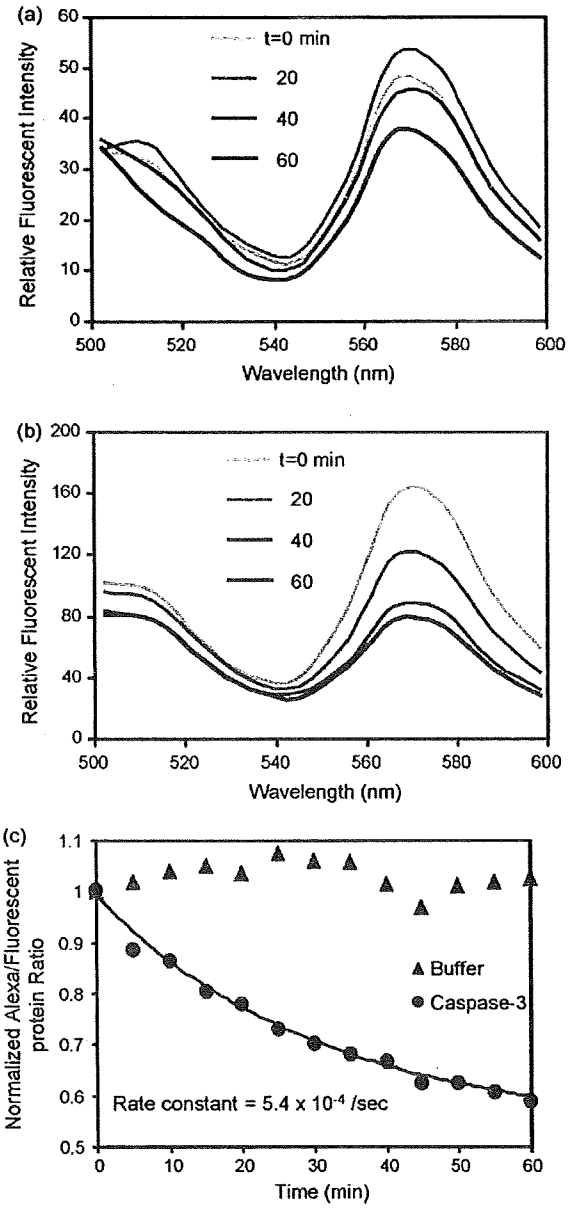

Fig. 2. Time course of caspase-3 digestion of NHGcas546 immobilized on the silicon surface. The fluorescence spectra of the immobilized NHGcas546 are overlaid (a, b). Immobilized NHGcas546 was incubated with (b) or without (a) 1 unit of recombinant caspase-3 for 60 min at room temperature on the silicon surface in 100-μL reaction solution. The fluorescence intensity of the immobilized NHGcas546 decreased in buffer solution alone (a). In contrast, the fluorescence intensity of Alexa Fluor 546 decreased in a time-dependent manner in caspase-3 solution (b). (c) First-order kinetic plot of the data from (a) and (b). The normalized ratio of the emission intensities for Alexa Fluor 546 (577–599 nm) and fluorescent protein (513–534 nm) is plotted. The points represent experimental data and the line shows the theoretical reaction kinetics determined by nonlinear least-squares regression fit to a first-order kinetic equation. Grey triangles indicate the ratio of the immobilized NHGcas546 in buffer solution, and the closed circles and black line indicate the ratio of the immobilized NHGcas546 treated with caspase-3 on the silicon surface.

The alteration of the ratio by caspase-3 digestion was larger when the NHGcas546 was free in solution (Fig. 1C, 7.4-fold) than when it was immobilized on the solid surface (Fig. 2c, 1.7-fold). One possible reason may be dysfunction of the NHGcas546 on the silicon surface caused by some denaturation during binding, which would decrease donor protein emission and consequently the efficiency of intramolecular FRET. A second possible reason may be

bleaching of the donor fluorescent protein by long-term continuous laser radiation of the target held on the solid surface, which could have a different effect than irradiation of the target in solution by the same laser. If we knew the critical point to detect some enzymatic reaction in the cell cycle or after some stimulation of the cell under study, we could avoid repeated visualization of the fluorescent probe. A third possible reason might be restricted access of caspase-3 to the immobilized NHGcas546 substrate by steric hindrance.

Next, we investigated the effect of caspase-3 concentration on the digestion of NHGcas546 on the silicon surface by changes in the ratio of donor and acceptor fluorescence emission as a routine indicator. The NHGcas546-modified silicon cantilever was treated with various amounts of caspase-3 in the reaction buffer for 30 min at 30 °C and observed by CLSM (LSM510-META) at 488 nm excitation and 513–599 nm emission. The normalized ratios of emission intensity of Alexa Fluor 546 (577–599 nm) to fluorescent protein (513–534 nm) were plotted against caspase-3 concentration (Fig. 3). The results suggested that the decay in the ratio of donor and acceptor emission intensities in response to enzyme concentration would be an adequate sensing system.

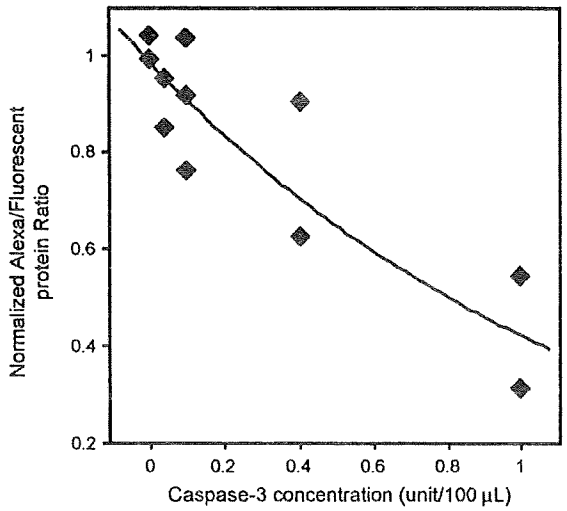

Fig. 3. Concentration-dependent caspase-3 digestion of immobilized NHGcas546 on the silicon surface. Immobilized NHGcas546 was treated with various amounts of caspase-3 for 30 min at 30 °C in 100-µL reaction solution. The normalized ratios of the emission intensities of Alexa Fluor 546 (577–599 nm) and fluorescent protein (513–534 nm) are plotted. Each mark indicates an individual experiment, and two or three experiments were performed for each caspase concentration. The line is the theoretical exponential curve derived by non-linear least-square regression fit to the plots.

3.4. Detection of caspase-3 activity in a single apoptotic cell

HeLa cells were treated with cycloheximide and TNF-α to induce apoptosis. After 2–3 h, the shape of the treated cells changed from oval to round, and apoptosis was initiated in the cells. The apoptotic cells were observed using CLSM (IX81/FV-1000) and the nanoneedle was moved toward an apoptotic cell using AFM (Fig. 4A).

Penetration of a cell with the nanoneedle can be monitored by observing a decrease or relaxation of the exerted force. Just after the nanoneedle comes in contact with the cell surface, the force on the nanoneedle increases due to resistance from indentation of the cell membrane and then suddenly decreases, indicating passage through the cell surface (Obataya et al., 2005c). After the nanoneedle travelled several µm, the force exerted on the NHGcas546-modified nanoneedle slightly increased and then flattened in the apoptotic cell (Fig. 4B). The force decreased further by about 1 nN and then flattened again. This result indicates that penetration of the probe-modified nanoneedle into an apoptotic cell was similar to penetration of a normal cell and was successfully done. The Young's modulus of the apoptotic cell was about 3.6 kPa; this value was less than the Young's modulus of normal HeLa cells (about 10 kPa). The probability of the nanoneedle being inserted

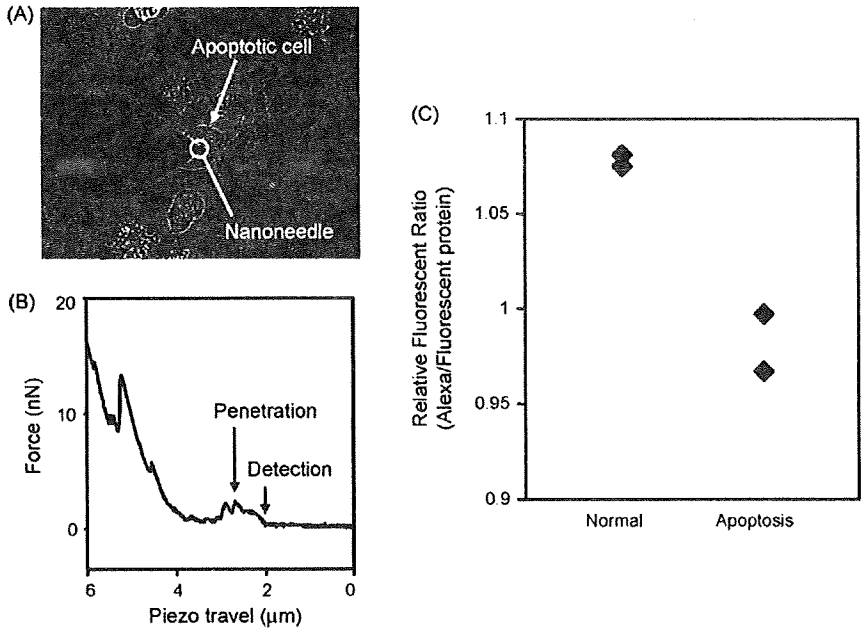

Fig. 4. Detection of caspase-3 activity in a single apoptotic cell. (A) Transmitted light image of cell manipulation using AFM. A round apoptotic cell was manipulated with the nanoneedle. (B) Force–distance curve of the nanoneedle during insertion into an apoptotic cell. The mechanical detection point and the point of penetration of the cell membrane by the nanoneedle are indicated. (C) The fluorescence ratio of NHGcas546 immobilized on the nanoneedle after insertion of the nanoneedle into a normal or apoptotic cell relative to the ratio before insertion. The NHGcas546-modified nanoneedle was maintained in the cell for 60 min at room temperature. The ratios of the normalized emission intensities of Alexa Fluor 546 (575–620 nm) and fluorescent protein (490–540 nm) are plotted.

into an apoptotic HeLa cell was over 90%. Thus, although the apoptotic cells became elastic, the probability of nanoneedle insertion was not affected by apoptosis.

To evaluate the activity of caspase-3 in apoptotic cells, the NHGcas546-modified nanoneedle was maintained inside an apoptotic cell for 60 min and the fluorescence ratios of the NHGcas546 on the nanoneedle were compared before and after insertion. The insertion of a nanoneedle with 400 nm diameter for more than 60 min does not induce lethal damage to the plasma membrane (Han et al., 2005). The fluorescence ratio decreased when the nanoneedle was inserted into apoptotic cells, but not normal cells (Fig. 4C). This result indicates successful detection of caspase-3 activation by apoptosis in a single cell using NHGcas546 immobilized on a nanoneedle.

Although we have succeeded in detecting the difference between normal and apoptotic cells by changes in the ratio, the decline of the ratio was smaller than in a previous study using chemically derived Alexa Fluor 532-modified UV5casS22tag incorporated into a single apoptotic HeLa cell, where they obtained a value which would be comparable to 0.6 in Fig. 4C (Suzuki et al., 2005). We need to consider several disadvantages of our immobilized probe system. As described in the previous section, the action of caspase-3 on the NHGcas546 probe free in solution produced a larger change in the fluorescence ratio than treatment of the same probe fixed on the silicon surface. In this study, a protein-based FRET probe was used because such probes could be highly applicable to detect many types of biological phenomena, including proteinase, kinase, or phosphatase action and changes in ion concentrations, pH, etc (Miyawaki, 2003; Sakaue-Sawano et al., 2008; Sato, 2006; Tsien, 2005). We will thus establish immobilization procedures that do not denature a protein-based probe and overcome bleaching of probes on the nanoneedle caused by continuous excitation.

The most commonly used methods for detecting apoptotic cells are the Annexin V assay and the TUNEL (TdT-mediated dUTP-biotin Nick End Labeling) assay. These methods can be used to detect apoptosis but not to continuously trace a single cell over time. FRET-based probes specific to caspase have been developed for detecting specific signal transduction during apoptosis (Takemoto et al., 2003; Tyas et al., 2000). These probes allow real-time monitoring of the enzyme activity in a single cell. However, the methods by which they are introduced into cells may cause invasive damage to the cells and cannot be applied to all cell types. Our newly devised MOMENT method involving the use of a micro-biosensor can be used for single cell analysis. Further, it can be used to specifically detect many types of biomolecules within various types of cells without causing invasive damage to the cells. In the future, we will refine this method so that it applications can be extended to many types of biomolecules.

4. Conclusions

As the demand for precise single cell manipulation to examine sequences of signal transduction increases, AFM has been intensively exploited as powerful tool in cellular and molecular biology (Lamontagne et al., 2008). In particular, AFM has been proposed to be useful for stimulation and for monitoring cellular homeostasis by introducing or extracting specific molecular entities from the cytoplasm of individual cells (Chen et al., 2007; Cuerrier et al., 2007; Han et al., 2005, 2008; Osada et al., 2003; Uehara et al., 2004). An AFM equipped with a nanoneedle would be a practical device to minimize the invasiveness of cell manipulation. This technique combined with fluorescent probes has great potential to reveal cellular states through investigating various intracellular phenomena. We have named this approach 'MOMENT'. To assess the feasibility of this approach, a new fluorescent probe for caspase-3 activity suitable for the AFM system was developed and used to detect caspase-3 activity induced in a single cell model system. Successful detection of enzymatic activity according to the cellular state suggested that this combination could be expanded to monitor many types of intracellular phenomena.

Acknowledgements

This study was partially supported by grants from the Ministry of Education, Culture, Sports, Science and Technology of Japan (Research and Development in a New Converting Field Based on Nanotechnology and Materials Sciences to JM and 19770163 to TK).

Appendix A. Supplementary data

Supplementary data associated with this article can be found, in the online version, at doi:10.1016/j.bios.2009.05.036.

References

Chen, X., Kis, A., Zettl, A., Bertozzi, C.R., 2007. Proc. Natl Acad. Sci. U.S.A. 104 (20), 8218–8222.
Cuerrier, C.M., Lebel, R., Grandbois, M., 2007. Biochem. Biophys. Res. Commun. 355 (3), 632–636.
Goda, T., Konno, T., Takai, M., Moro, T., Ishihara, K., 2006. Biomaterials 27 (30), 5151–5160.
Han, S., Nakamura, C., Obataya, I., Nakamura, N., Miyake, J., 2005. Biochem. Biophys. Res. Commun. 332 (3), 633–639.
Han, S.W., Nakamura, C., Kotobuki, N., Obataya, I., Ohgushi, H., Nagamune, T., Miyake, J., 2008. Nanomedicine 4 (3), 215–225.
Ishihara, K., Nomura, H., Mihara, T., Kurita, K., Iwasaki, Y., Nakabayashi, N., 1998. J. Biomed. Mater. Res. 39 (2), 323–330.
Ishihara, K., Ziats, N.P., Tierney, B.P., Nakabayashi, N., Anderson, J.M., 1991. J. Biomed. Mater. Res. 25 (11), 1397–1407.
Kihara, T., Yoshida, N., Mieda, S., Fukazawa, K., Nakamura, C., Ishihara, K., Miyake, J., 2007. NanoBiotechnology 3 (2), 127–134.
Kitano, H., Imai, M., Mori, T., Gemmei-Ide, M., Yokoyama, Y., Ishihara, K., 2003. Langmuir 19 (24), 10260–10266.
Konno, T., Watanabe, J., Ishihara, K., 2004. Biomacromolecules 5 (2), 342–347.
Lamontagne, C.A., Cuerrier, C.M., Grandbois, M., 2008. Pflugers Arch. 456 (1), 61–70.
Miyawaki, A., 2003. Dev. Cell 4 (3), 295–305.
Moro, T., Takatori, Y., Ishihara, K., Konno, T., Takigawa, Y., Matsushita, T., Chung, U.I., Nakamura, K., Kawaguchi, H., 2004. Nat. Mater. 3 (11), 829–836.
Obataya, I., Nakamura, C., Han, S., Nakamura, N., Miyake, J., 2005a. NanoBiotechnology 1 (4), 347–352.
Obataya, I., Nakamura, C., Han, S., Nakamura, N., Miyake, J., 2005b. Biosens. Bioelectron. 20 (8), 1652–1655.
Obataya, I., Nakamura, C., Han, S., Nakamura, N., Miyake, J., 2005c. Nano Lett. 5 (1), 27–30.
Ormo, M., Cubitt, A.B., Kallio, K., Gross, L.A., Tsien, R.Y., Remington, S.J., 1996. Science 273 (5280), 1392–1395.
Osada, T., Uehara, H., Kim, H., Ikai, A., 2003. J. Nanobiotechnol. 1 (1), 2.
Pollok, B.A., Heim, R., 1999. Trends Cell Biol. 9 (2), 57–60.
Sakaue-Sawano, A., Kurokawa, H., Morimura, T., Hanyu, A., Hama, H., Osawa, H., Kashiwagi, S., Fukami, K., Miyata, T., Miyoshi, H., Imamura, T., Ogawa, M., Masai, H., Miyawaki, A., 2008. Cell 132 (3), 487–498.
Sato, M., 2006. Anal. Bioanal. Chem. 386 (3), 435–443.
Suzuki, M., Ito, Y., Sakata, I., Sakai, T., Husimi, Y., Douglas, K.T., 2005. Biochem. Biophys. Res. Commun. 330 (2), 454–460.
Suzuki, M., Ito, Y., Savage, H.E., Husimi, Y., Douglas, K.T., 2003. Chem. Lett. 32 (3), 306–307.
Suzuki, M., Ito, Y., Savage, H.E., Husimi, Y., Douglas, K.T., 2004. Biochim. Biophys. Acta 1679 (3), 222–229.
Takemoto, K., Nagai, T., Miyawaki, A., Miura, M., 2003. J. Cell Biol. 160 (2), 235–243.
Thornberry, N.A., Rano, T.A., Peterson, E.P., Rasper, D.M., Timkey, T., Garcia-Calvo, M., Houtzager, V.M., Nordstrom, P.A., Roy, S., Vaillancourt, J.P., Chapman, K.T., Nicholson, D.W., 1997. J. Biol. Chem. 272 (29), 17907–17911.
Tsien, R.Y., 2005. FEBS Lett. 579 (4), 927–932.
Tyas, L., Brophy, V.A., Pope, A., Rivett, A.J., Tavare, J.M., 2000. EMBO Rep. 1 (3), 266–270.
Uehara, H., Osada, T., Ikai, A., 2004. Ultramicroscopy 100 (3-4), 197–201.
Voldman, J., 2006. Curr. Opin. Biotechnol. 17 (5), 532–537.
Yang, F., Moss, L.G., Phillips Jr., G.N., 1996. Nat. Biotechnol. 14 (10), 1246–1251.

Current Applied Physics 9 (2009) e291–e293

Contents lists available at ScienceDirect

Current Applied Physics

journal homepage: www.elsevier.com/locate/cap

Mechanical role of the nucleus in a cell in terms of elastic modulus

Toshihiro Sugitate [a], Takanori Kihara [a,b,*], Xue-Ying Liu [a], Jun Miyake [a,b,c]

[a] Department of Bioengineering, School of Engineering, The University of Tokyo, 7-3-1, Hongo, Bunkyo-ku, Tokyo 113-8656, Japan
[b] Center for NanoBio Integration, The University of Tokyo, 7-3-1, Hongo, Bunkyo-ku, Tokyo 113-8656, Japan
[c] Department of Mechanical Science and Bioengineering, Graduate School of Engineering Science, Osaka University, 1-3, Machikaneyama, Toyonaka, Osaka 560-8531, Japan

ARTICLE INFO

Article history:
Received 31 March 2009
Received in revised form 8 June 2009
Accepted 14 June 2009
Available online 18 June 2009

PACS:
87.17.Rt

Keywords:
AFM
Young's modulus
Membrane penetration
Nucleus
Actin cytoskeleton

ABSTRACT

Mechanical properties of cells reflect their unique physiological status. Methods for direct measurement of these properties and their applications are required for cell therapy and diagnostics. Young's modulus of the cell and nuclear surfaces of human mesenchymal stem cells (hMSCs) were measured using atomic force microscopy with a cone-shaped probe. Young's moduli of the cell surface and bare exposed nuclear surface of hMSCs were 54.3 ± 37.37 kPa and 1.11 ± 0.58 kPa, respectively. The height of the bare nucleus was three times greater than that of an intact cell. Although the normal cell surface showed membrane penetrability with the cone-shaped probe, the bare nucleus was impenetrable. By de-polymerizing the actin filaments, Young's modulus of the hMSCs was reduced to 3.05 ± 2.77 kPa, and the height of the cell increased such that it was similar to that of the bare nucleus. Disruption of the actin cytoskeleton makes the cell surface impenetrable. However, the nuclear structure maintains the penetrability of cell membrane in an actin de-polymerized cell. Rigidity and penetrability of the cell membrane are maintained by the actin cytoskeleton, and the nuclear structure supports the cell surface under conditions of actin de-polymerization.

1. Introduction

Analysis of mechanical parameters provides unique or specific information about a material of interest. In the case of cells, the mechanical properties of biological components, such as the cell membrane, cytoskeleton, and cytosol reflect the unique physiological status of the cell. Therefore, methods for mechanically measurement cell properties and their application to cell therapy and diagnostics are required.

Some techniques such as poking with micropipette [1,2] as well as the use of a laser optical tweezer [3,4] or atomic force microscopy (AFM) [5] have been adopted to measure cell mechanical properties. In particular, AFM has been used extensively to study the mechanical properties of a cell. Elastic properties of a living cell can be analysed using AFM by the probe indentation method [4,6–8], stress relaxation method [9], and force modulation method [10].

Surface mechanical properties of a cell are mainly defined by the actin cytoskeleton [1–4,8]. Furthermore, the structures of organelles are very complicated and these will affect mechanical properties of the cell. In fact, the nucleus of cell plays an important role as a central support for maintaining the cell body and as an anchor for cell motility [10]. Moreover, analysis of the viscoelastic properties of the nucleus revealed that it was significantly stiffer and more viscous than intact chondrocytes [11]. Nevertheless, it is not known whether or not the mechanical properties of the cell surface are defined by the physical characteristics of the cell nucleus.

In this study, we investigated influence of the cell nucleus on the mechanical properties of the cell surface by comparing the physical properties of a bare exposed nucleus and an actin de-polymerized cell.

2. Materials and methods

2.1. Materials

The AFM cone-shaped silicon probe (ATEC-CONT, 0.02–0.75 N/m) was purchased from Nanosensors (Neuchatel, Switzerland). Human bone marrow derived mesenchymal stem cells (hMSCs; obtained from a 19-year-old male, #6F4393) were purchased from Lonza Inc. (Walkersville, MD). Other reagents were purchased from Wako Pure Chemical Industries Ltd. (Osaka, Japan), Invitrogen (Carlsbad, CA), or Sigma–Aldrich (St. Louis, MO).

2.2. Cell culture

hMSCs were maintained in alpha-MEM containing 0.5% L-glutamate, 15% FBS, and antibiotics (100 units/mL penicillin G, 100 μg/mL streptomycin sulphate, and 25 μg/mL amphotericin B) at 37 °C in a humidified atmosphere of 5% CO_2 and 95% air. hMSCs from

* Corresponding author. Address: Department of Bioengineering, School of Engineering, The University of Tokyo, 7-3-1, Hongo, Bunkyo-ku, Tokyo 113-8656, Japan. Tel./fax: +81 3 5841 0246.
E-mail address: takanori.kihara@gmail.com (T. Kihara).

1567-1739/$ - see front matter © 2009 Elsevier B.V. All rights reserved.
doi:10.1016/j.cap.2009.06.020

seven passages were used in this study. Actin de-polymerization of hMSC was induced by treatment with 1 μM cytochalasin D for 1 h.

2.3. Exposure of the nucleus

The cell nucleus was exposed by semi-pressing the cell between cover glasses in the medium. hMSCs cultured on a cover glass were semi-pressed with another cover glass, and the surface of the plasma membrane was peeled off by removing the upper cover glass from the cell. The exposure of the nuclei was confirmed by microscopic observation.

2.4. Measurement of Young's modulus

hMSCs or nuclei on the cover glass were placed on a glass bottom dish containing Opti-MEM and manipulated using AFM (Nanowizard I, JPK Instruments AG, Berlin, Germany). The cone-shaped probe was indented into the material up to 20 nN at 10 μm/s. The Young's modulus of the cell and the nucleus was calculated in accordance with the Hertz model. The force–distance curve at the region of indentation of the material surface was fitted to the Hertz model. The following equation was used in the Hertz model of indentation for the cone-shaped indenter:

$$F = \frac{E}{(1-\nu^2)}\frac{2\tan\alpha}{\pi}I^2,$$

where, F = force, I = depth of indentation, α = semi-opening angle of the cone, ν = Poisson's ratio (0.5), and E = Young's modulus.

All examinations were performed in 10 cells or nuclei at room temperature.

3. Results and discussion

3.1. Membrane penetration of the cone-shaped AFM probe

hMSCs adhered to and well spread on the cover glass. The cone-shaped probe was moved towards a cell or nucleus using AFM. Typical force–distance curves obtained from the indentation of the surface of the cell or nucleus with the probe are shown in Fig. 1. Just after the probe came into contact with the cell or nuclear surface, the force on the probe increased due to resistance from indentation of the cell or nuclear membrane (Fig. 1a). The force frequently decayed by approximately 300 pN and then increased again (Fig. 1a). This force decay is due to membrane penetration of the sharp probe tip during indentation [12].

The frequency of penetration of the hMSC membrane with the probe on the nucleus was 8 of 10 and that with the probe in the surrounding nuclear area was almost the same (Fig. 1c). In case of only the bare nucleus, the force–distance curve profile was different from that of normal hMSCs (Fig. 1b). The force slowly increased during indentation of the nuclear surface, and force decay was not observed (Fig. 1b). Thus, the nuclear membrane could not be penetrated with the cone-shaped probe. To consider the contribution of the actin cytoskeleton to cell membrane penetration, actin filaments of the hMSC were de-polymerized by treatment with cytochalasin D. Although the frequency of membrane penetration in the actin de-polymerized cell measured on the nucleus was 8 of 10, the frequency measured in the surrounding nuclear area was only 1 of 10 (Fig. 1c).

The plasma membrane of the hMSCs could be penetrated with the cone-shaped probe. However, the actin de-polymerized cell membrane could not be penetrated in the surrounding nuclear area. Thus, the actin cytoskeleton is fundamental to membrane penetration with a cone-shaped probe. The bare nuclear membrane, which is originally located under the cell membrane, also could not be penetrated with the cone-shaped probe, whereas

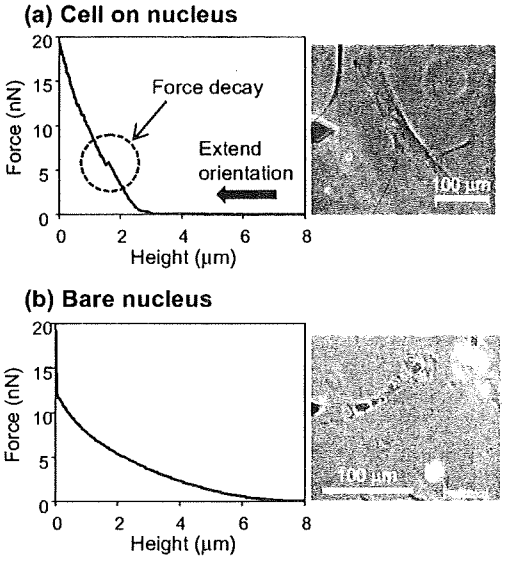

(c) Frequency of appearance of force decay

Target material	Frequency
Cell on nucleus	8/10
Cell in the surrounding nucleus area	7/10
Bare nucleus	0/10
Actin de-polymerized cell on nucleus	8/10
Actin de-polymerized cell in the surrounding nuclear area	1/10

Fig. 1. Typical force–distance curves obtained from the indentation of the surface of each material with the cone-shaped AFM probe. The probe indents the cell surface on the nucleus (a) or the surface of the bare nucleus (b). Force–distance curve (graph on the left) and microscopic image of the target cell or nucleus (right). The force decay point is indicated. (c) Frequency of appearance of force decay in each target cell or nucleus.

the cell membrane on the nucleus could be penetrated with this probe with and without actin de-polymerization treatment.

These results suggest that membrane penetration requires a structure for membrane-support. Although the lamina structure is known to bind to chromatin fiber in the nucleus, the nuclear membrane does not have a supporting structure, but a native nucleus can support an actin de-polymerized cell surface.

3.2. Cell height

In our measurement condition, the measured cell or nuclear height was not accurate, because the probe was retracted at a 20 nN repulsive force. However, we can roughly estimate the cell or nuclear height. The cell height of hMSCs was approximately 2.8 μm and the nuclear height was approximately 7.1 μm (Fig. 2A). The nuclear height of the hMSCs was around three times higher than that the cell height. Due to the destruction of the cell structure, the constraints on the nucleus are removed and it expands due to surface tension. Actin de-polymerization induced morphological change, namely, an increase in the cell height to a level similar to that of the nucleus (Fig. 2A). This suggested that the lamina structure of the native nucleus supports the cell body even under conditions of fragmentation of actin filaments.

3.3. Young's moduli of cell and nuclear surfaces

Young's moduli of the cell surface of hMSCs was 54.3 ± 37.4 kPa with the probe on the nucleus and 69.3 ± 35.7 kPa with the probe in the surrounding nuclear area (Fig. 2B). A large standard deviation (above 50%) of Young's modulus indicated that each individual

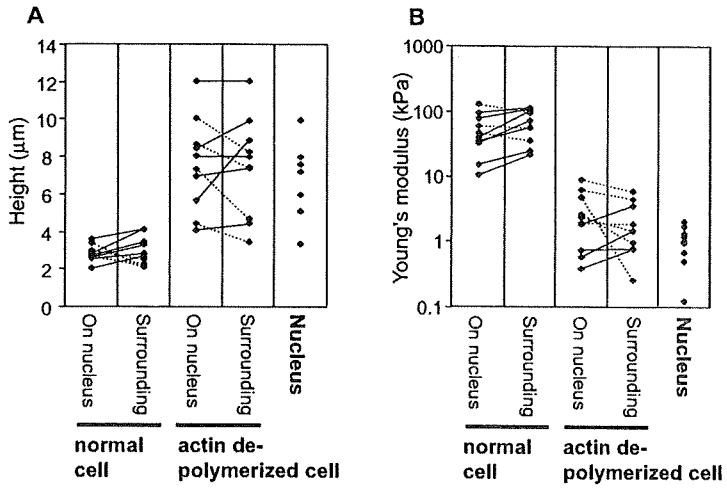

Fig. 2. Height (A) and Young's moduli (B) of normal hMSCs, actin de-polymerized hMSCs, and bare nuclei. The cone-shaped probe was indented towards the cell surface on the nucleus (on nucleus) or in the surrounding nuclear area (surrounding). Each point indicates an individual experiment. The points joined by a line indicate the same cell. The solid line shows the cell in which the value in the case of the surrounding nuclear area is higher than that on the nucleus, and the dashed line shows the cell in which the value in the case of the surrounding nuclear area is lower.

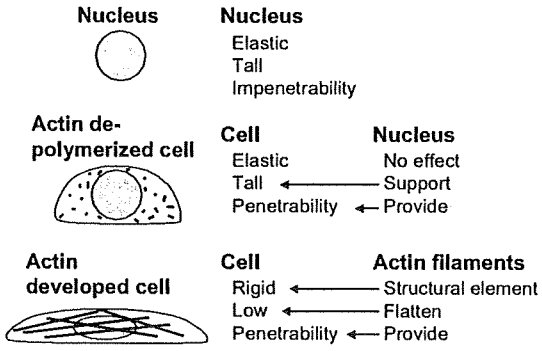

Fig. 3. Schematic diagrams of the effect of the nucleus and actin cytoskeleton on the cell surface properties.

cell of the same cell type has a unique cell stiffness. In each individual cell, Young's modulus measured on the nucleus was lower than that measured in the surrounding nuclear area (Fig. 2B). Young's modulus of the bare nuclear surface was 1.11 ± 0.58 kPa and it was significantly lower than that of the native cell surface (Fig. 2B). When hMSCs were treated with cytochalasin D, Young's modulus of the cell surface measured on the nucleus and in the surrounding nuclear area were dramatically reduced to 3.05 ± 2.77 kPa and 2.14 ± 1.84 kPa, respectively (Fig. 2B).

The native cell surface structure is apparently maintained by the actin cytoskeleton. The Young's modulus of the actin de-polymerized cell surface, however, was hardly distinguishable from that of the nuclear surface. The large Young's modulus of the actin de-polymerized cell surface may be due to the influence by the actin fiber fragments (Fig. 2B).

3.4. Effect of the nucleus and actin cytoskeleton on the cell surface properties

Schematic diagrams of the effect of the nucleus and actin cytoskeleton on the cell surface properties is shown in Fig. 3. The bare nucleus is very elastic and impenetrable, and the height of nucleus is large. Actin filaments flatten the cell and nucleus resulting in a decrease in the height of a normal cell. Due to de-polymerization of the actin filaments in a cell, the constraints on the nucleus are removed and it expands due to surface tension and lamina structure. The nucleus supports the cell surface when the actin cytoskeleton is fragmented.

The rigidity and penetrability of the cell membrane is controlled by the actin cytoskeleton. Disruption of the actin cytoskeleton changes the physiological properties of the cell membrane making it soft and impenetrable. The nuclear structure, however, maintains the penetrability of the cell membrane in the case of an actin de-polymerized cell. Thus, the nuclear structure supports the cell surface in an actin de-polymerized cell.

4. Conclusion

Our study aimed at examining the mechanical properties of cell and nuclear surfaces of hMSCs using AFM equipped with a cone-shaped probe. The normal cell surface showed a highly Young's modulus and membrane penetrability. On the other hand, a very low elastic modulus and impenetrability were obtained in the case of a bare nucleus. Fragmentation of the actin cytoskeleton changes the physiological properties of the cell surface making it soft and impenetrable. However, the nuclear structure maintains the penetrability of the cell membrane and supports the cell surface in an actin de-polymerized cell. The rigidity and penetrability of the cell membrane is maintained by the actin cytoskeleton, and the nuclear structure supports the cell surface under conditions of actin de-polymerization.

Acknowledgements

This study was partially supported by grants from the Ministry of Education, Culture, Sports, Science and Technology of Japan (Research and Development in a New Converting Field Based on Nanotechnology and Materials Sciences to JM and 19770163 to TK).

References

[1] W.R. Trickey, T.P. Vail, F. Guilak, J. Orthop. Res. 22 (2004) 131–139.
[2] F. Guilak, G.R. Erickson, H.P. Ting-Beall, Biophys. J. 82 (2002) 720–727.
[3] I. Titushkin, M. Cho, Biophys. J. 90 (2006) 2582–2591.
[4] I. Titushkin, M. Cho, Biophys. J. 93 (2007) 3693–3702.
[5] M. Radmacher, IEEE Eng. Med. Biol. Mag. 16 (1997) 47–57.
[6] A.B. Mathur, G.A. Truskey, W.M. Reichert, Biophys. J. 78 (2000) 1725–1735.
[7] Y. Rabinovich, M. Esayanur, S. Daosukho, K. Byer, H. El-Shall, S. Khan, J. Colloid Interface Sci. 285 (2005) 125–135.
[8] A.M. Collinsworth, S. Zhang, W.E. Kraus, G.A. Truskey, Am. J. Physiol. Cell Physiol. 283 (2002) C1219–C1227.
[9] E.M. Darling, S. Zauscher, J.A. Block, F. Guilak, Biophys. J. 92 (2007) 1784–1791.
[10] M. Nagayama, H. Haga, K. Kawabata, Cell Motil. Cytoskel. 50 (2001) 173–179.
[11] F. Guilak, J.R. Tedrow, R. Burgkart, Biochem. Biophys. Res. Commun. 269 (2000) 781–786.
[12] I. Obataya, C. Nakamura, S. Han, N. Nakamura, J. Miyake, Biosens. Bioelectron. 20 (2005) 1652–1655.